Undergraduate Research Newsletter
University of Miami

MIAMI

Volume 5 ~ October 2022

EDITORS

REVIEW BOARD

Special Thanks

Office of Undergraduate Research and Community Outreach

Available Online: For more information please visit the URN homepage at https://chemistry.as.miami.edu/research-groups/captain-research-group/undergraduate-research-newsletter-urn/index.html

Table of Contents

	Page
Modification of surface functional groups of carbon nitride carbon dots for more efficient drug delivery and cancer selectivity ***Jordan M. Garber***	1
The process of obtaining photoactivatable BODIPY and its role in the biomedical field ***Mia Lenardos***	7
Resonant conditions for hyperfine-assisted quantum tunneling of a particle through a delta well scatterer embedded in a potential barrier ***Karna Nagalla***	9
Inhibition of pancreatic cancer by Homoharringtonine, a protein translation elongation inhibitor ***Cataryna Rodriguez***	12

Foreword

Research is an essential component of undergraduate education. Moving the first steps in a laboratory environment may be intimidating. Learning the many techniques required to design, perform and interpret an experiment may be overwhelming. The thrill and excitement for scientific discovery, however, generally overwhelms the initial hesitance of the laboratory novice. The trepidation that always accompanies a successful experiment is in fact the addicting ingredient that eventually encourages students to purse research-oriented career paths.

Designing, performing and interpreting an experiment is just a mere sequence of three steps that must be reiterated over and over to develop an entire project from beginning to end. The hard work in the laboratory should ideally advance science and possibly have an impact on society. In turn, such an outcome demands divulgation of successful experimental results, and perhaps even of failures, to the scientific community with a formal mechanism. Background, hypothesis, results, conclusions and, possibly, some suggestions on future directions must all be communicated concisely in written form. Undergraduate students performing research, however, are not really exposed to the daunting task of crafting a scientific publication, which, just like experimental work, requires practice and dedication. The Undergraduate Research Newsletter (URN), edited by Dr. Captain, provides students with the invaluable opportunity of venturing, for the first time, into the arts and crafts of manuscript composition.

This URN issue collects four contributions. Three of them are at the interface of biomedical and chemical research. They report the development of innovative bioimaging probes, based on either large carbon particles or small organic molecules, and protein inhibitors for pancreatic cancer. The fourth explores quantum tunneling effects. I would like to congratulate the four authors for their brilliant contributions and hope these articles to be the first of many more to come in successful research-oriented careers.

Dr. Françisco M. Raymo

Professor of Chemistry

Modification of surface functional groups of carbon nitride carbon dots for more efficient drug delivery and cancer selectivity

Jordan M. Garber (Class of 2024)

Major: Chemistry
Principial Investigator: Dr. Roger M. Leblanc
Department: Chemistry

Since the discovery of carbon quantum dots (CDs) in 2004, they have earned an exceedingly distinguished reputation for being the forefront agent in nanomedicine [1, Vol. 28]. Carbon dots are excellent candidates for bioimaging, biosensing, and drug delivery with exceptional biocompatibility, high photoluminescence (PL), and astonishing tunable surface functionality. Carbon dots diverge from traditional quantum dots as CDs are innocuous and both green and economical to produce. Two established methods to synthesize CDs are (1) a bottom-up approach and (2) a top-down approach. In the bottom-up approach, organic precursors are ionized to form radicals, ions, and electrons, which condense into clusters of aromatic structures, while the top-down approach deteriorates a pure carbon source into a powder and then further into ultra-small clusters of compounds [2, pp. 565–586]. In the top-down approach, a chemical, electrochemical, electrolysis, acid, reflux, or laser ablation can be used to degrade the carbon source into CDs [2]. CDs, correspondingly, possess a unique ability to incorporate an organic percussor as a surface, functional group, allowing CDs to be remarkable cell targeting agents.

As carbon nitride carbon dots, abbreviated CNDs, have been previously synthesized and extensively characterized in a former study conducted by our research group, CNCs exhibited enough promising pharmacological and biological application to substantiate a deeper study. This study assessed the surface functional group tunability of CNDs. By manipulating the amounts of precursors, it is hypothesized to yield a carbon dot with more sought qualities. It is hypothesized that the condensation reaction occurs when the amine group of a urea molecule attacks the electrophilic site of the terminal carboxylic group of a citric acid molecule. As the reaction site is ionized and heated further, this nucleophilic attack of the carbonyl group leads to a polyamide formation which carbonizes (Fig. 1). Since modified CNDs follow the same condensation reaction. Because CNDs have previously been synthesized, a revised yet comprehensive protocol was designed to assure purity and varying ratios of surface functional groups. Since it is imperative for any sample of carbon dots to be pure because impurities (e.g., excess reactants or fluorophores) interfere with optical properties and biocompatibility, three distinct purification steps: (1) centrifugation, (2) syringe filtration, and (3) dialysis were integrated into the synthesis of different ratios of CNDs [3, pp. 111–123]. These CNDs were synthesized using a bottom-up approach, specifically, a microwave-mediated approach. Once both 0.5 g of citric and 0.5 g, 1.5 g, and 2.5 g of urea was dissolved in 25 mL of DI water, the solution was vigorously stirred overnight to prepare 1:1, 1:3, and 1:5 CND ratios, respectively. The solution was ionized and heated using a standard domestic microwave for 7 minutes at 700W. After the black, solid residue was dispensed in 15 mL of DI water, the sample was sonicated for 30 minutes. To collect a pure sample, the CND samples were centrifuged, and the supernatant was extracted twice for 15 minutes at 1500 rpm. The sample was then purified using a syringe filtration with a filter membrane of 0.2 μm.

The filtrate underwent dialysis for three days with a dialysis tubing with a MWCO of 100-500 Da. The remaining water after dialysis was vaporized by heating to approximately 75°C.

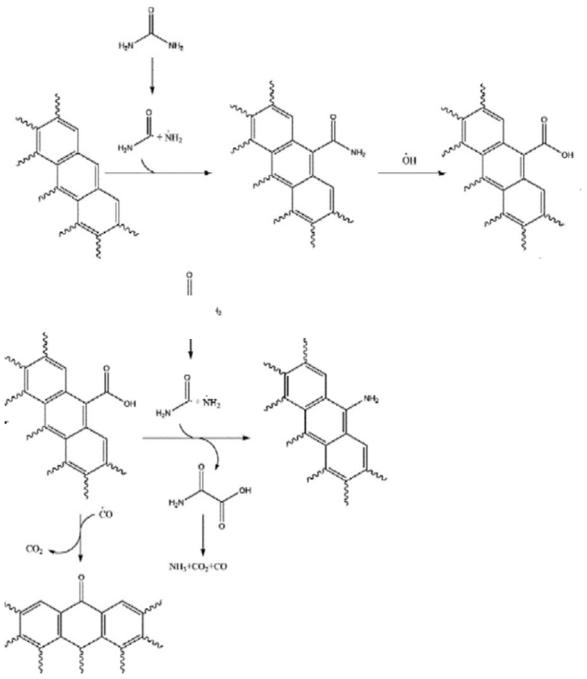

Figure 1. The synthesis reactions of CNDs Schematic representation of radical carboxylation of CND edges.

The governing principle behind this experiment is to selectively modify the surface of CNDs for a larger and deeper investigation, requiring the chemical and biochemical qualities to be examined. The CNDs were initially characterized with UV-vis spectroscopy. The CNDs displayed characteristic bands between 200-400nm (Fig. 2). When CNDs were previously investigated, the peaks were assigned to be both n-π* electronic transitions of carbonyl groups and π- π* electronic transition of carbon nitride s-triazine rings [3, pp. 111–123]. Since both 1:3 and 1:5 CNDs differ in surface structure, the prominent peak at 412 nm is designated as a n-σ* and n-π* electronic transition of C-N and C=N groups respectively [4, pp. 1770251-n/a]. Although 1:1 CNDs vastly differ from both 1:3 and 1:5 CNDs, both 1:3 and 1:5 CNDs share dominant absorption bands of peaks at 252, 271, 327, and 355 nm, contributing to the n-π* electronic transitions of carbonyl groups.

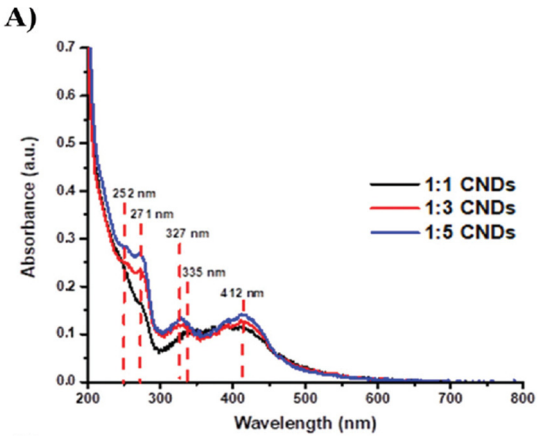

Figure 2. UV–vis absorption spectra of modified CNDs (concentration = 0.1 mg/mL)

Photoluminescence (PL) spectroscopy furthered the differentiation among the different ratios of CNDs. As both 1:3 and 1:5 CNDs experienced a red shift when they were excited at 350 or 375 nm, the 1:3 CNDs produced maximum peaks at 498 nm and 507 nm when excited at 350 nm or 375 nm, respectively (Fig. 3C), while 1:5 possessed maximum bands at 501 nm and 507 nm when excited at 350 nm or 375 nm, respectively (Fig 3D). The 1:1 CNDs retained maximum peaks at 442 and 483 nm when excited at 350 or 375 nm, respectively (Fig 3B).

Fourier transform infrared (FTIR) illustrated the varying amounts of surface functional groups. As 1:1 CNDs presented a prominent peak at 3026 cm^{-1}, pertaining to ν_{O-H} from a carboxylic group, both 1:3 and 1:5 CNDs did not. Both 1:3 and 1:5 CNDs continued to differ from 1:1 CNDs as 1:3 and 1:5 CNDs peaked at 1690 cm^{-1}, concerning $\nu_{C=O}$ from an amide group. The FTIR scans of both 1:3 and 1:5 CNDs, conversely, undoubtedly explains how 1:3 and 1:5 CNDs

have less COOH and more C(O)NH2 groups. The remaining FTIR bands peaking at 3185, 2761, 1776, 1592, 1414, 1361, 1290, 1181, 1047, and 766 cm^{-1} were assigned to ν_{N-H}, ν_{O-H}, $\nu_{C=O}$, $\nu_{C=C}$, δ_{C-H}, δ_{O-H}, ν_{C-O}, ν_{C-N}, ν_{C-O}, and s-triazine, respectively (Fig. 4) [5, pp. 485–497], [6, pp. 502–520], [7, pp. 875–880].

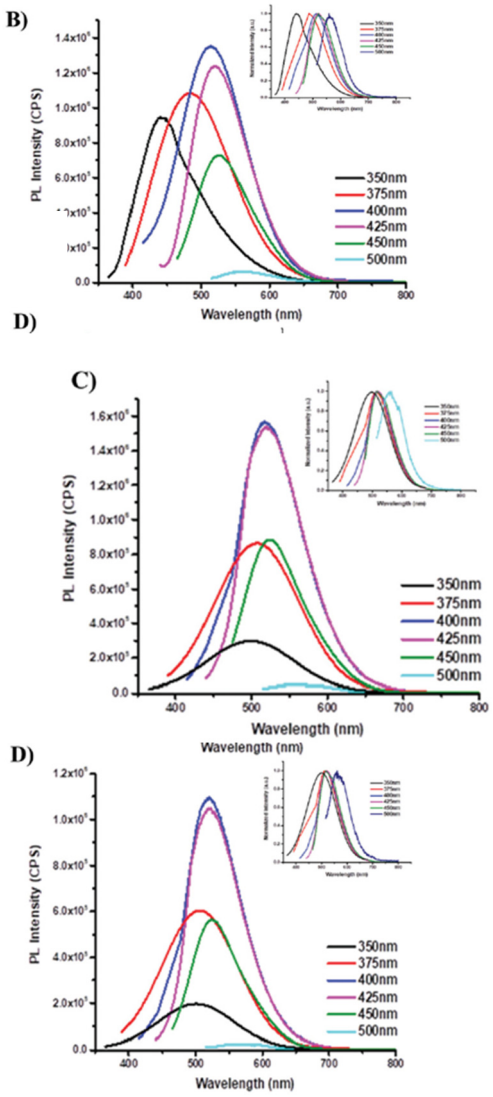

Figure 3 (B–D). PL emission spectrum of 1: 1, 1: 3, 1: 5 CNDs (concentration = 1 x 10^{-6} mg/mL), respectively. Insets, normalized PL emission spectra of 1: 1, 1: 3, 1: 5 CNDs

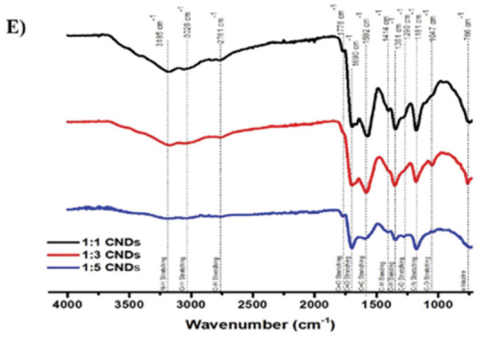

Figure 4. FTIR spectra of modified CNDs.

The average PL quantum yield (QY) was used to determine if different ratios possessed different levels of photoelement properties. The mean quantum yield (Φ) was achieved by computing the quantum yield (Φ) against each standard using:

$$\Phi = \Phi_r \times \frac{I}{I_R} \times \frac{A_R}{A} \times \left(\frac{n_R}{n}\right)^2$$

where Φ_R, I, A, n represent the literature quantum yield of a standard, the integrated area under the fluoresce curve, the absorbance intensity at 350 nm, and the refractive index, respectively; R is designated for values of the standards. Despite the average PL quantum yield (QY) being calculated, they did not vary substantially. The 1:1, 1:3, and 1:5 CNDs had a QY of 12%, 13%, and 10% respectively. AFM and TEM studies were used to evaluate both morphological and the size distribution of CNDs. As collected in a previous study, 1:1 CNDs maintain a diameter between 2.0 and 3.5 nm with a height between 1.0 and 3.8 nm [3, pp. 111–123]. While 1:3 CNDs had an average height profile between 1.6-2.0 nm (Fig S1A) with a diameter of 2.7-3.1 nm (Fig S1B), the 1:5 CNDs had an average height profile between 1.3-2.1 nm (Fig S1C) with a diameter 2.7-3.2 nm (Fig S1D). CNDs, generally, share common height profiles and average diameters, verifying a spherical shape. It is worth noting that there is no

significant change in size or morphology of different ratios of citric acid and urea. To illustrate and differentiate the surface composition of CNDs, the zeta potential measurements revealed how 1:1, 1:3, and 1:5 CNDs exhibited surface charges of 38.8, 23.4, and 20.4 mV, respectively (Fig. 3A). As mentioned in a previous section, it is expected that the particle's molar mass of different ratios of CNDs should be the same as they are synthesized in the same condensation reaction. MALDI-TOF, a form of mass spectroscopy, confirms that for 1:1, 1:3, and 1:5, CND ratios have a M+ peak at 750 (Fig 3A), validating that although CNDs were synthesized with varying amounts of precursors, they are synthesized by the same mechanism.

The quantification of surface functional groups was examined by two different assays. A simple acid-base, gravimetric titration quantified surface carboxylic group with 0.1M NaOH. It is assumed that the carbon dots act as strong acids, making the equivalence point at the pH of 7. It was found that per gram of 1:1, 1:3, and 1:5 CNDs, there were 0.30, 0.20, and 0.18 mmol of surface -COOH groups, respectively. A fluoresceine assay supportively confirmed that the surface -NH2 groups per gram of 1:1, 1:3, and 1:5 CNDs were 0.007 mol, 0.010 mol, and 0.024 mol, respectively. The quantitative data here confirms the observations seen in the FTIR absorbance peaks, varying the amounts of the percussor does change the concentrations of both surface amine and carboxylic groups.

After detailed and extensive characterization and quantification of surface groups of CNDs, different ratios CNDs nanocarrier abilities were examined. CNDs were conjugated with doxorubicin, a commonly prescribed chemotherapeutic. It is widely accepted that doxorubicin has severe side effects on nontumor cells [8, pp. 296–310]. The intention behind using a nanocarrier over just the standard drug is how nanocarriers selectively target and deliver drugs to help limit the side effects.

Sample	QY (%) ± STD	Number of surface -COOH groups (mmol/g)	Number of surface -NH_2 groups (mmol/g)	Zeta Potential (mV)	MALDI-TOF +1 Ionization Main Peak (m/z)
1:1 CNDs	12 ± 2.0	0.30	0.007	-33.8	750
1:3 CNDs	12 ± 2.1	0.20	0.010	-23.4	750
1:5 CNDS	10 ± 1.8	0.18	0.024	-20.4	750

Figure 5. Table for quantum yield, number of –COOH and –NH_2 groups on the surface, surface charge and MALDI-TOF main +1 ionization peak of1: 1:1, 1:3, and 1:5 CNDs

A successful conjugation between CNDs and doxorubicin with a carbodiimide with an EDC/NHS bioconjugation. The UV-vis absorption spectra of 1:1, 1:3, and 1:5 CNDs conjugated with doxorubicin (CNDs-Dox) exposed how the conjugation was successful. Since both doxorubicin and 1:1, 1:3, and 1:5 CNDs-Dox have an absorption band at 490 nm, the conjugation was deemed successful. The quantification of the amount of doxorubicin was found using a technique developed in our research group. [9, pp. 14773–14777] The technique involves creating a calibration curve based on a compound's chirality. The governing principle of this technique is circular dichroism (CDH). Using a doxorubicin calibration curve, the amount of doxorubicin-loaded onto 1:1, 1:3, and 1:5 CNDs were 0.41, 0.51, and 0.52 μmol/g (Fig. 6). Despite a decreasing amount of surface COOH groups as the ratio of CNDs increases, the isoelectric point (pI) of the molecule determines the amount loaded. Moreover, molecules with a higher pI are accepted as a base, decreasing the efficiency of EDC/NHS

conjugations with structures that donate COOH groups [10, pp. 9972–99728]. Since doxorubicin's pI is 8.40, doxorubicin is classified as a basic structure. Therefore, since 1:1 CNDs have the highest negative surface charge, it results in more repulsions and lower coupling ability with doxorubicin, explain how 1:1 CNDs have the lowest amount loaded.

Sample	Amount of doxorubicin loaded per mg of conjugate (µmol/g) ± STD
1:1 CNDs-Dox	0.41 ± 0.03
1:3 CNDs-Dox	0.51 ± 0.03
1:5 CNDs-Dox	0.52 ± 0.03

Figure 6. The amount of doxorubicin loaded on to modified CNDs

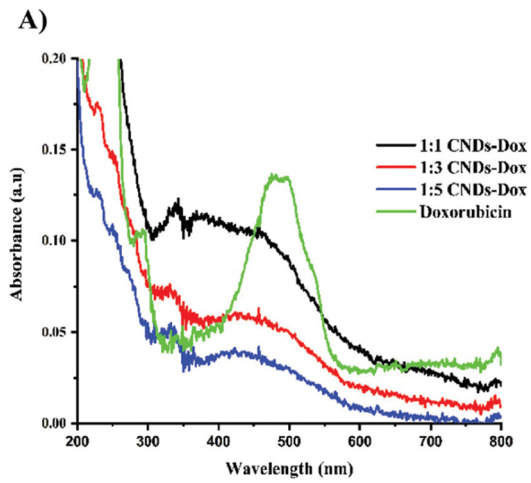

Figure 7. UV-vis absorption spectra of Dox, 1:1 CND–Dox, 1:3 CND–Dox and 1:5 CND–Dox conjugates

Throughout the duration of this study, surface modified CNDs were successfully synthesized by varying the amounts of precursors. After characterizing modified CNDs, increased amount of urea as a percussors leads to more -NH_2 groups. Various spectroscopic and microscopic techniques displayed modified CNDs' optical, size, morphology, and both surface functionality and charge. To apply modified CNDs to biological systems, a carbodiimide coupling mechanism was employed to conjugate doxorubicin onto CNDs to form CND-Dox conjugates. Both 1:3 and 1:5 CNDs surface charge was more favorable for loading doxorubicin because of their surface charge. In retrospect, this study delivers both the chemical and biological effect of surface functional groups of nanocarriers. The results of this study allows further applications for personalized nanomedicine for diverse types of cancers by engineering a specific carbon dot with desired surface functional groups.

References

1] V. Ţucureanu, A. Matei, and A. M. Avram, "FTIR Spectroscopy for Carbon Family Study," vol. 46, no. 6, pp. 502–520, Nov. 2016, doi: 10.1080/10408347.2016.1157013. [Online]. Available: https://www.tandfonline.com/doi/abs/10.1080/10408347.2016.1157013

[2] X. Yang *et al.*, "Hyaluronic acid/EDC/NHS-crosslinked green electrospun silk fibroin nanofibrous scaffolds for tissue engineering," vol. 6, no. 12, pp. 9972–99728, Oct. 2016, doi: 10.1039/c6ra13713j.

[3] B. C. L. . Ferreira, P. Y. Liyanage, and R. M. Leblanc, "Drug Loading of Anthracycline Antibiotics on Carbon Dots Using Circular Dichroism Spectrometry," vol. 93, no. 44, pp. 14773–14777, Nov. 2021, doi: 10.1021/acs.analchem.1c03385. [Online]. Available: http://dx.doi.org/10.1021/acs.analchem.1c03385

[4] X. Cao *et al.*, "A facile microwave-assisted fabrication of fluorescent carbon nitride quantum dots and their application in the detection of mercury ions," vol. 151, pp. 875–880, Dec. 2015, doi: 10.1016/j.saa.2015.07.034. [Online]. Available: https://dx.doi.org/10.1016/j.saa.2015.07.034

[5] E. Kirbas Cilingir *et al.*, "Metformin derived carbon dots: Highly biocompatible fluorescent nanomaterials as mitochondrial targeting and blood-brain barrier penetrating biomarkers," vol. 592, pp. 485–497, Jun. 2021, doi: 10.1016/j.jcis.2021.02.058. [Online]. Available: https://dx.doi.org/10.1016/j.jcis.2021.02.058

[6] P. Y. Liyanage *et al.*, "Carbon Nitride Dots: A Selective Bioimaging Nanomaterial," vol. 30, no. 1, pp. 111–123, Jan. 2019, doi: 10.1021/acs.bioconjchem.8b00784. [Online]. Available: http://dx.doi.org/10.1021/acs.bioconjchem.8b00784

[7] M. Nasrollahzadeh, M. S. Sajadi, M. Atarod, M. Sajjadi, and Z. Isaabadi, *An Introduction to Green Nanotechnology*, vol. 28. San Diego: Elsevier Science & Technology, 2019 [Online]. Available:

https://ebookcentral.proquest.com/lib/[SITE_ID]/detail.action?docID=5716907
[8] U. Kanwal, N. Irfan Bukhari, M. Ovais, N. Abass, K. Hussain, and A. Raza, "Advances in nano-delivery systems for doxorubicin: an updated insight," vol. 26, no. 4, pp. 296–310, Apr. 2018, doi: 10.1080/1061186X.2017.1380655. [Online]. Available: https://www.tandfonline.com/doi/abs/10.1080/1061186X.2017.1380655
[9] F. Yuan, S. Li, Z. Fan, X. Meng, L. Fan, and S. Yang, "Shining carbon dots: Synthesis and biomedical and optoelectronic applications," vol. 11, no. 5, pp. 565–586, Oct. 2016, doi: 10.1016/j.nantod.2016.08.006. [Online]. Available: https://dx.doi.org/10.1016/j.nantod.2016.08.006
[10] B. van Dam *et al.*, "Carbon Dots: Excitation-Dependent Photoluminescence from Single-Carbon Dots (Small 48/2017)," vol. 13, no. 48, pp. 1770251-n/a, Dec. 2017, doi: 10.1002/smll.201770251. [Online]. Available: https://onlinelibrary.wiley.com/doi/abs/10.1002/smll.201770251

The process of obtaining photoactivatable BODIPY and its role in the biomedical field

Mia Lenardos (Class of 2024)

Major: Chemistry
Principal Investigator: Dr. Françisco Raymo
Department: Chemistry

The purpose of our research was to make photoresponsive compounds that have the properties of self-assembling nanoparticles of amphiphilic polymers that can transport hydrophilic molecules across hydrophilic media. As a result, these compounds are extremely valuable delivery agents for a diversity of biomedical applications such as for fluorescence imaging.

These photoresponsive compounds are a combination of borondipyrromethene (BODIPY) chromophore and photocleavable oxazine within their covalent skeleton. As seen in Figure 1, under illumination at an activation wavelength, "the oxazine ring cleaves irreversibly to bring the adjacent BODIPY fragment in conjugation with an indole heterocycle" (Zhang et al.).[1]

This action allows for the photoactivation 2qwZbrightness and contrast. This inventive structure of BODIPY allows for activatable fluorophores with superb photophysical and photochemical properties.

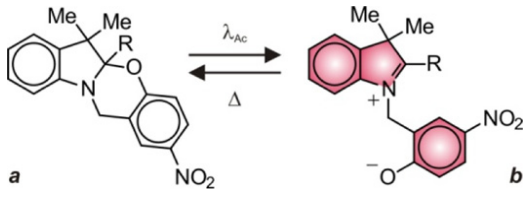

Figure 1. Opening of an oxazine ring (a) to form a zwitterionic isomer (b) under illumination at an activating wavelength**.**

During my time in the lab, I was able to help conduct the experiments to produce BODIPY. As seen in Figure 2, the synthesis to produce pure BODIPY is quite extensive and difficult.

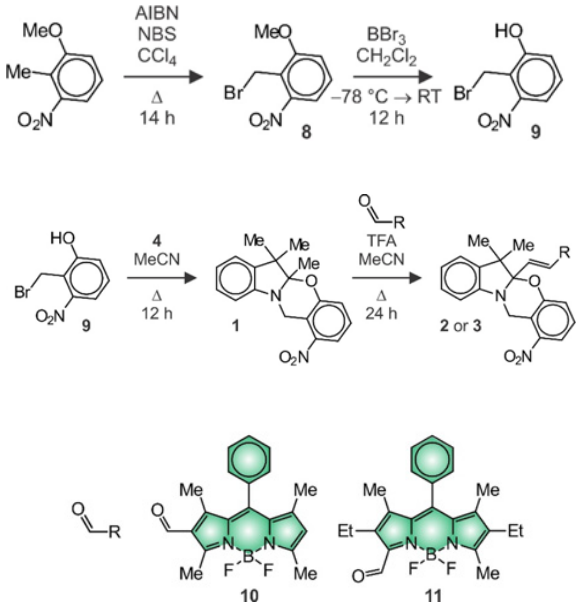

Figure 2. The synthesis of BODIPY.

Column chromatography was used to separate the mixture from remaining reagents or contaminating substances. Many vials were used in the collection of BODIPY and it was interesting that the colors of the mixtures in the vials spanned from green, orange, red, and even brown. As it can be seen in Figure 3, thin layer chromatography (TLC) was used to identify which vials contained pure BODIY by comparing them to the stock BODIPY solution. In this specific picture, vials 1A through 1G are thought to contain only pure BODIPY; whereas, vials 1I through 2G may contain other substances besides BODIPY.

Lastly, Nuclear Magnetic Resonance (NMR) was used to confirm that we had obtained pure BODIPY.

Unfortunately, during my time in the lab so far, we have not been able to obtain pure BODIPY. We have had hope through

successful-looking TLC plates, but when the NMR results are obtained one observed other components in the solution. There are tremendous opportunities for future work in relations to the study of BODIPY. As stated earlier, the application of using BODIPY for an abundance of biomedical applications is in the near future.

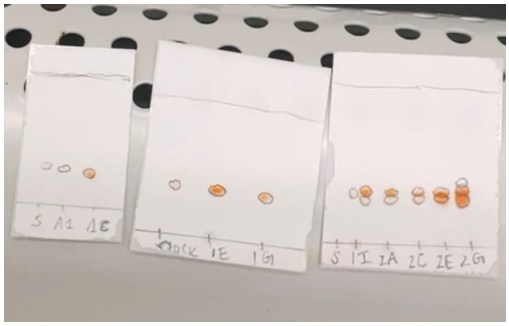

Figure 3. Thin layer chromatography of stock BODIPY and comparing vials**.**

References

[1] Zhang Y., Swaminathan S., Tang S., Garcia-Amorós J., Boulina M., Captain B., Baker J. D., Raymo F. M. Photoactivatable BODIPYs designed to monitor the dynamics of supramolecular nanocarriers. Journal of the American Chemical Society 2015, 137, 4709-19.

Resonant conditions for hyperfine-assisted quantum tunneling of a particle through a delta well scatterer embedded in a potential barrier

Karna Nagalla (Class of 2023)

Major: Chemistry and Applied Mathematics
Principle Investigator: Jamie D. Walls, Ph.D
Department: Chemistry

The tunneling probabilities for a particle with energy E incident to a potential defined by a rectangular barrier of height V_0 and length $2L$ and embedded with a single delta well scatterer of "strength" α located at the center of the barrier were investigated (Figure 1). Resonance equations that provide the conditions for which an incoming particle perfectly penetrates the potential with 100% transmission were derived.

Tunneling is a purely quantum mechanical phenomenon whereby an incident particle with energy below a classically impenetrable potential barrier can penetrate and be transmitted through the barrier. This phenomenon is a direct consequence of wave-particle duality, i.e., an object behaving as both a wave and a particle. Our project models the scenario whereby an electron may tunnel through a barrier containing a nuclear spin that can couple to the electron's spin via the hyperfine Fermi contact interaction.

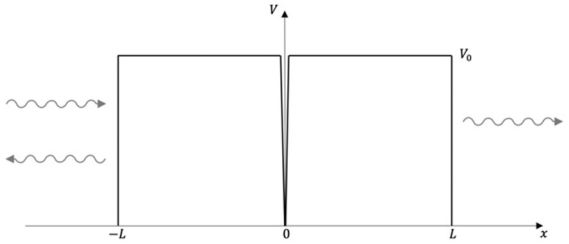

Figure 1. Model of the potential. The height of the barrier is V_0. The central divot represents the Dirac delta well of strength α at position $x = 0$. An incident plane wave from the left is either reflected (backwards arrow on left side) or has tunneled through the barrier (forward arrow on right side).

In the following discussion, the electron and nuclear spins are assumed to be aligned, in which case the hyperfine interaction resembles a potential Dirac delta potential well. To calculate the transmission probabilities through such a potential as shown in Figure 1, the time-independent Schrodinger equation is solved by breaking up the total wave function into the following four regions:

$$Region\ I = \{-\infty < x \leq -L\}$$

$$Region\ II = \{-L \leq x \leq 0\}$$

$$Region\ III = \{0 \leq x \leq L\}$$

$$Region\ IV = \{L \leq x < \infty\}$$

The general solution of the Schrodinger equation takes the form of a sum of positive and negative exponential functions multiplied by constants. In each region these would be given by:

$$\psi_I(x) = e^{ikx} + Re^{-ikx} \quad in\ region\ I$$

$$\psi_{II}(x) = Ce^{\kappa x} + De^{-\kappa x} \quad in\ region\ II$$

$$\psi_{III}(x) = Fe^{\kappa x} + Ge^{-\kappa x} \quad in\ region\ III$$

$$\psi_{IV}(x) = Te^{ikx} \quad in\ region\ IV$$

where R and T are the reflection and transmission coefficients, respectively.

In solving a tunneling problem, one is interested in the constant corresponding to the wavefunction of Region IV (T) which is used to compute the transmission probability ($|T|^2$). A property of the wavefunction is that it and its first derivative are both continuous between Regions I and II, and Regions III and

IV. Due to the delta-potential, however, the first derivative of the wave functions between Regions II and III is discontinuous.[1] With this constraint, we solve for the constants. From the solution to the Schrodinger equation, the transmission ($|T|^2$) and reflection ($|R|^2$) probabilities are obtained.

Resonance equations for a potential dictate when perfect transmission through the potential occurs (i.e. the transmission probability $|T|^2$ goes to 1). To calculate the resonance equations for our potential, we suspected that they could be derived by observing the known resonance equations for an analogous potential. The double barrier is similar to the potential we consider (Figure 1) though instead of a dividing delta well, the barriers are split apart by a width w. The resonance condition of this potential is:

$$\frac{d}{dw}(|T|^2)^{-1} = 0$$

where $|T|^2$ is the transmission probability of the double barrier problem.[3] Applying the condition to that transmission probability simplifies into transcendental resonance equations.[2,3] These can be numerically evaluated to determine the resonance energies at which incoming particles perfectly tunnel through the potential structure. If one considers the limiting case of the double barrier where the width between the barriers vanishes (i.e. $w \to 0$), the single barrier case is recovered. For the potential we investigate, the single barrier case is recovered if the delta well vanishes (i.e. the hyperfine constant $\alpha \to 0$), so it was hypothesized the resonance equations could be derived by applying the following resonance condition:

$$\frac{d}{d\alpha}(|T|^2)^{-1} = 0$$

We simplified the result into transcendental equations and confirmed their validity numerically (Figure 2).

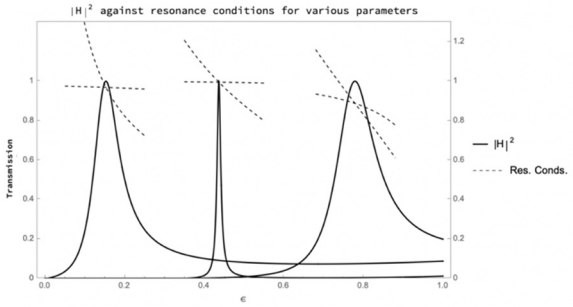

Figure 2. $|T|^2$ for various parameters (solid curves) are plotted with resonance equations (dotted lines) against the energy ratio $\epsilon = E/V_0$ where E is the energy of the incoming particle and V_0 is the height of the barrier (i.e. $0 \leq \epsilon \leq 1$).

The intersections of the resonance equations correspond to the peaks of the transmission curves. The domains of the transcendental equations for each case of parameters are truncated for clarity.

In conclusion, our investigation revealed the transmission coefficient for the central delta well scatterer embedded in a barrier which can be used to model electronic hyperfine-assisted tunneling. We were also able to determine transcendental equations for when resonant tunneling through the barrier can occur. In our further investigations we would like to determine other properties of this system such as the width of resonance transmission peaks, the range of α values at which resonances can occur, and also extend our study to a model electronic tunneling through N nuclei (i.e. N delta well scatterers embedded randomly in a barrier).

References

[1] D. J. Griffiths and D. F. Schroeter, (2020). *Introduction to quantum mechanics*. Cambridge University Press.
[2] V. E. Sakhnyuk, A.M. Shutovskyi, S.A. Fedosov, *and* O.V. Zamuruyeva, "The resonant condition of transmission in the graphene-based double-barrier structures", Low Temperature Physics 48,806-810 (2022)
[3] V. S. Olkhovsky et al "Resonant and non-resonant tunneling through a double barrier", 2005 EPL 70 712

Inhibition of pancreatic cancer by Homoharringtonine, a protein translation elongation inhibitor

Cataryna Rodriguez (Class of 2024)

Major: Microbiology and Immunology & Public Health
Principle Investigator: Dr. Sundaram Ramakrishnan
Co-Mentors: Janneth Maria Oleas , Arunkumar Rengaraj
Department: Department of Surgery and Sylvester Comprehensive Cancer Center

Currently, pancreatic cancer patients are treated with neoadjuvant or adjuvant chemotherapy. Most of the currently used chemotherapies target either the DNA synthesis (e.g. Gemcitabine) or microtubule stability (Paclitaxel) or cell signaling pathways (e.g. receptor tyrosine kinase inhibitors). In the present studies we determined the efficacy of a ribosomal inhibitor, Homoharringtonine, on pancreatic ductal adenocarcinoma (PDAC). Cytotoxic effects of Homoharringtonine (HHT), which inhibits translation elongation, was determined on Pancreatic cancer cell proliferation in vitro and tumor angiogenesis in vivo. HHT is an alkaloid isolated from the evergreen tree, Cephalotaxus harringtonia which is native to southern China. It binds to ribosomal A-site and interferes with correct positioning of aminoacyl-tRNA and thereby, inhibits translocation of tRNA to the P-site of the ribosome during protein synthesis. Our data show that HHT inhibits human pancreatic cancer cell line (PANC1) and mouse pancreatic cancer cell line (KPC) very efficiently at nanomolar concentration. Furthermore, HHT blocked proliferation of Gemcitabine resistant PANC1 cells. In addition, HHT was found to inhibit a mouse colon cancer cell line, MC-38 as well. Then we evaluated whether HHT could inhibit tumor angiogenesis in mice. KPC-induced angiogenesis of Matrigel plugs was significantly reduced by HHT treatment at a dosing of 0.7 mg/kg. In summary, protein translation elongation inhibitor HHT, is effective in inhibiting pancreatic cancer cell proliferation. Gemcitabine resistant pancreatic cancer cells are sensitive to HHT. PDAC angiogenesis was effectively inhibited by HHT treatment.

Protein synthesis (translation) is essential for cancer cell survival, tumor growth and metastasis. Three major steps are involved in protein synthesis; translation initiation, translocation and termination. A number of natural products and synthetic compounds have been found to inhibit protein synthesis (Figure 1). Translation initiation is for example inhibited by Silvestrol, Rapamycin and 4Gi. HHT by virtue of its binding to ribosome A-site, it prevents translocation and peptide elongation. Inhibition of protein synthesis prevents cells from progressing through the G1 phase into the S phase as well as from the G2 phase into the M phase[2]. HHT is currently being evaluated for treating chronic myeloid leukemia, myelodysplastic syndrome, and acute myeloid leukemia[2]. FDA has approved the use of HHT to treat chronic myeloid leukemia patients after they fail to respond to two or more tyrosine kinase inhibitors[1]. Moreover, other studies are underway to determine the effects of HHT on other cancers like hepatocellular carcinoma[3].

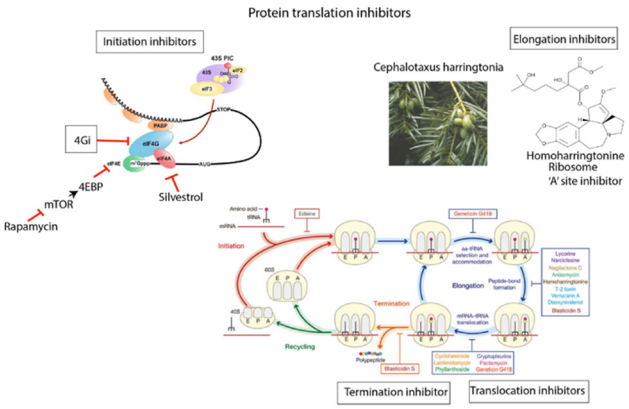

Figure 1. Inhibitors of proteins synthesis and structure of HHT.

To contribute to the undergoing studies involving the effect of HHT on other cancers, my study mainly focuses on determining the efficacy of HHT on pancreatic ductal adenocarcinoma (PDAC) while also conducting some studies regarding HHT's effects on colon cancer. To carry out this project, we did a series of experiments. First, mouse pancreatic cancer cell line (KPC), human pancreatic cancer cell line (PANC1), and mouse colon cancer cell line (MC38) were seeded in 96-well plates and treated with varying concentrations of HHT. After 48 hours, cell viability was determined by CCK8 kit and Gemcitabine controls were used to compare the relative potency of HHT. Secondly, real-time cell proliferation was determined in xCelligene by measuring changes in electrical impedance in control and HHT-treated cultures. Lastly, the effect of HHT on tumor cell-induced angiogenesis was determined using matrigel plug assay. Frozen sections (15 µM) were prepared from control and HHT treated samples and fixed in cold acetone. Sections were then stained with rat anti-mouse CD31-PE conjugate. Images were captured in Leica microscope and analyzed for vessel density by morphometry.

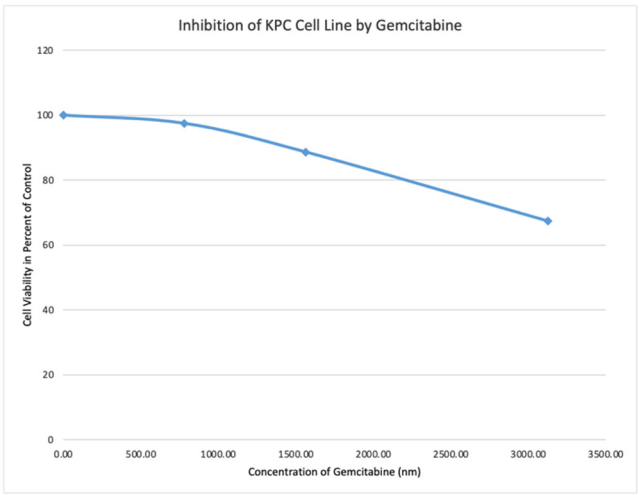

Figure 2. The inhibition of mouse pancreatic cancer cell line (KPC) by Gemcitabine. It served as a positive control and showed an IC50 (inhibitory concentration 50) of 3500 nM.

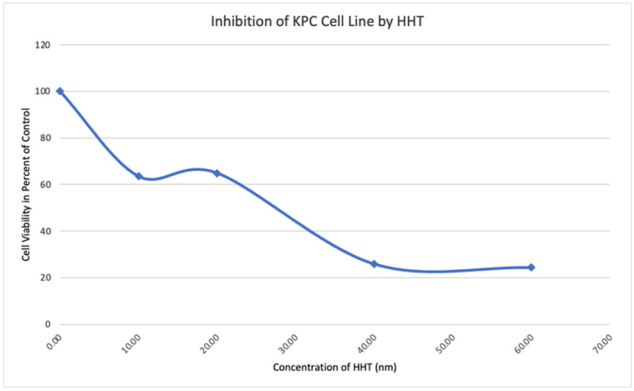

Figure 3. The inhibition of mouse pancreatic cancer cell line (KPC) by HHT. Each value is a mean of quadruplicate cultures. Mouse pancreatic cancer cell line was more sensitive to HHT with an IC50 of 22 nM.

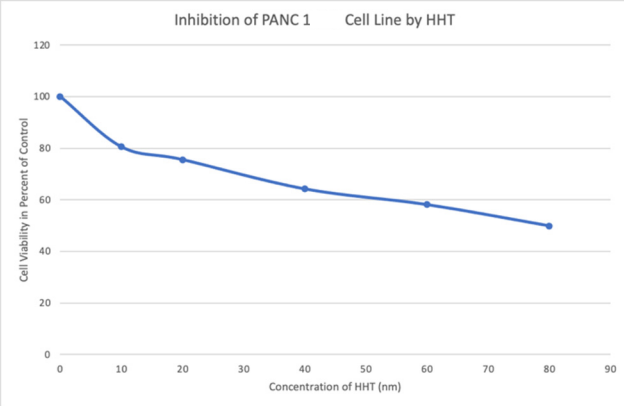

Figure 4. The inhibition of human pancreatic cancer cell line (PANC1) by HHT. The IC50 for PANC1 cells was calculated to be around 109 nM.

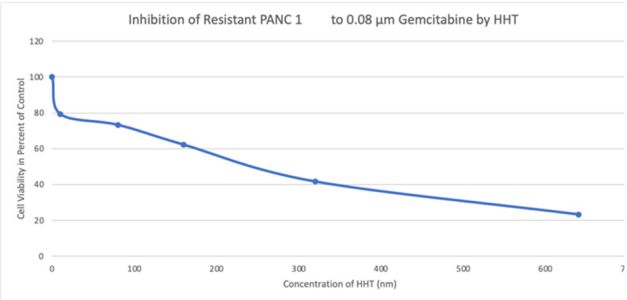

Figure 5. The inhibition of Gemcitabine resistant human pancreatic cancer (PANC1) by HHT. The drug-resistant cells (0.08 uM Gemcitabine) were inhibited by HHT with an IC50 of 220 nM.

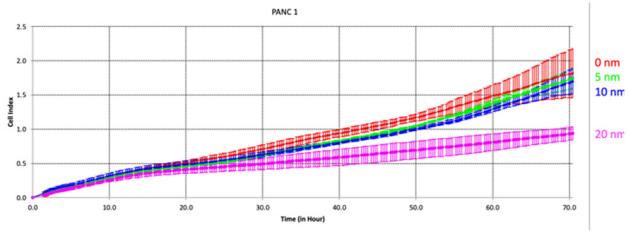

Figure 6. Cell proliferation inhibition of human pancreatic cancer cell line (PANC1) by HHT.

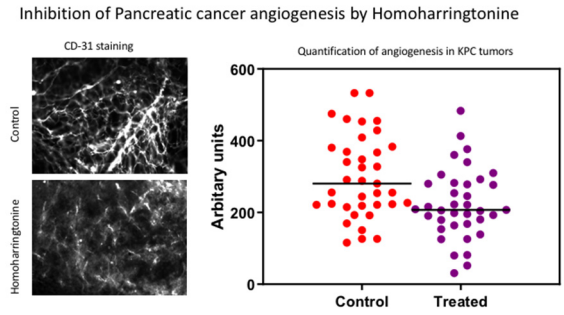

Figure 7. Inhibition of KPC-induced angiogenesis by HHT. CD-31 staining shows blood vessels. Data from morphometric analyses is shown in the right panel.

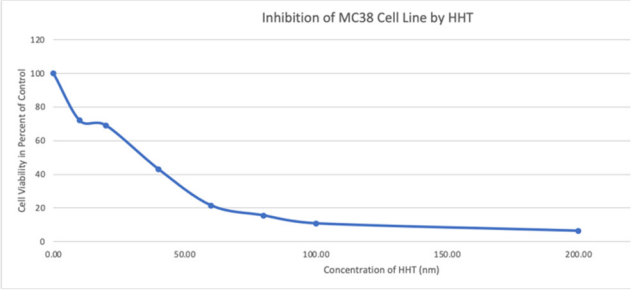

Figure 8. The inhibition of mouse colon cancer cell line (MC38) by HHT.

Our data show that HHT treatment inhibits human pancreatic cancer cell line, PANC1, and mouse pancreatic cancer cell line, KPC, with an IC50 of 109 nM (Figure 4) and 22 nM (Figure 3) respectively. In addition, HHT was found to be highly cytotoxic to a mouse colon cancer cell line, MC 38, (Figure 8) and efficiently blocked proliferation of Gemcitabine resistant PANC1 with an IC50 of 220 nM (Figure 5). Also, KPC-induced angiogenesis of Matrigel plugs was significantly reduced by HHT treatment at a dosing of 0.7 mg/kg (Figure 7). Therefore, HHT was found to be a potent inhibitor of pancreatic cancer cells in vitro and was cytotoxic to mouse and human cancer cell lines. Moreover, Gemcitabine resistant human pancreatic

cancer cells were found to be sensitive to HHT-mediated cytotoxicity. HHT inhibited pancreatic cancer cell-induced angiogenesis in vivo.

Our future studies will focus on evaluating anti-tumor activity of HHT in preclinical models of pancreatic and colon cancers as well as determining the impact of HHT on immunotherapy against pancreatic cancer in mouse models.

References

[1] Kantarjian, H. M., O'Brien, S., & Cortes, J. (2013). Homoharringtonine/Omacetaxine Mepesuccinate: The Long and Winding Road to Food and Drug Administration Approval. *Clinical Lymphoma, Myeloma & Leukemia*, *13*(5), 530–533. https://doi.org/10.1016/j.clml.2013.03.017

[2] Zhou, D. C., Zittoun, R., & Marie, J. P. (1995). Homoharringtonine: An effective new natural product in cancer chemotherapy. *Bulletin Du Cancer*, *82*(12), 987–995.

[3] Zhu, M., Gong, Z., Wu, Q., Su, Q., Yang, T., Yu, R., Xu, R., & Zhang, Y. (2020). Homoharringtonine suppresses tumor proliferation and migration by regulating EphB4-mediated β-catenin loss in hepatocellular carcinoma. *Cell Death & Disease*, *11*(8), 1–13. https://doi.org/10.1038/s41419-020-02902-2